RESEARCH ARTICLE | JUNE 07 2021

Genetic algorithm optimization for storing arbitrary multimode transverse images in thermal atomic vapor

Yun Chen; Chengyuan Wang ✉; Ya Yu; ... et. al

Check for updates

CrossMark

View Online

Export Citation

Articles You May Be Interested In

Joint Inversion of Multimode Love Wave Dispersion Curves for Accurately Appraising of Shear Wave Velocity Reversal Profile

AIP Conference Proceedings (July 2010)

Design of a wideband multimode tonpilz transducer with a nonuniform piezoelectric layer stack

J Acoust Soc Am (October 2011)

Optimization of the performance of a voltage measuring station using genetic algorithm

Rev Sci Instrum (June 2021)

Genetic algorithm optimization for storing arbitrary multimode transverse images in thermal atomic vapor

View Online   Export Citation   CrossMark

Yun Chen,[1] Chengyuan Wang,[1,a)] (iD) Ya Yu,[1] Zibin Jiang,[1] Jinwen Wang,[1,2] (iD) Shupeng Zhao,[1] Dong Wei,[1] Hong Gao,[1,a)] (iD) and Fuli Li[1]

AFFILIATIONS

[1]MOE Key Laboratory for Nonequilibrium Synthesis and Modulation of Condensed Matter, Shaanxi Province Key Laboratory of Quantum Information and Quantum Optoelectronic Devices, School of Physics, Xi'an Jiaotong University, Xi'an 710049, China
[2]School of Physics and Astronomy, University of Glasgow, Glasgow G12 8QQ, United Kingdom

a)Authors to whom correspondence should be addressed: wcy199202@gmail.com and honggao@mail.xjtu.edu.cn

ABSTRACT

Storing multimode transverse images in atomic media is crucial in constructing large-scale quantum networks. A major obstacle of storing transverse images in the thermal atomic vapor is the distortion of the retrieved images caused by atomic diffusion. Here, we demonstrate the combination of genetic algorithm with the phase-shift lithography method to construct the optimal phase for an arbitrary transverse image that can diminish the effect of diffusion. Theoretical simulations and experimental results manifest that the retrieved images' resolution can be substantially improved when carrying the optimal phases. Our scheme is efficient and straightforward and can be extensively applied in storing complex transverse multimodes in diffusion media.

Published under an exclusive license by AIP Publishing. https://doi.org/10.1063/5.0053849

Coherent storage and manipulation of light with different degrees of freedom (DOF) are essential for building quantum repeater based large-scale quantum networks.[1–4] Notably, storing the transverse multimode DOF is of great value in constructing multiplexed quantum repeaters with high information processing speed.[5,6] The transverse multimodes generally include spatially structured light fields, e.g., Laguerre–Gaussian modes,[7] Ince–Gaussian modes,[8,9] light fields with complex polarization distribution,[10] and transverse images.[11] Until now, a lot of works on storing transverse multimodes have been reported in media, such as crystal,[3,12] cold atomic ensemble,[13–15] and thermal atomic vapor.[11,16,17] Among these media, the thermal atomic vapor cell exhibits the advantages of having a low cost and sizeable cross-sectional window, allowing it to possess greater transverse multimode storage capacity.[5]

Nevertheless, the thermal atomic motion-induced diffusion[18] severely decreases the quality of retrieved transverse multimode,[18–20] especially the transverse image with a complicated spatial profile. In order to diminish the impact of atomic diffusion on the retrieved image, several methods have been proposed, such as the optical phase-shift lithography technique,[21] storing Fourier transform of the image,[11] correlation imaging technique,[16] storing Bessel–Gauss beams and Bessel speckles.[22] When storing images with a large size and complex spatial profile, the storage performance under the method in Ref. 11 is unsatisfactory because the atomic diffusion attenuates the outer parts of the image. The methods in Refs. 16 and 22 are valid only for specific light fields and are not universal. The optical phase-shift lithography technique[21] is based on flipping the adjacent regions' phase of an image, such that atoms diffusing to the areas between the regions will interfere destructively. Then, the retrieved image will maintain a clearer outline. Theoretically, for an arbitrary image to be stored, one can load it with an elegant phase structure based on the phase-shift lithography method to resist image blurring caused by atomic diffusion. Since Shuker *et al.* first utilized this technique to increase the spatial resolution of a stored three-line pattern,[21] the storage of general images with more complex spatial distribution based on this technique has not been further elaborated. The main reason is that it is difficult to directly derive the appropriate phase distribution for an image with complicated spatial profiles.

However, if this problem is to be considered as a mathematical model that can be solved by intelligent optimization algorithms, the solution process would be more concise and explicit. Genetic algorithm (GA)[23] has the advantages of fast convergence and strong

robustness to noise, and it provides a general framework for solving the optimal solution of complex system, e.g., scattering media,[24–26] molecular geometry,[27] cold atom.[28] In this Letter, we demonstrate theoretically and experimentally the GA's application for constructing the optimal phases of arbitrary images and investigate the performance of the optimal phase for diminishing the effect of diffusion on the stored complex transverse images.

Let us begin by describing the mathematical model and the framework of GA for constructing the optimal phase. During the storage process, the envelope of the probe beam $\mathbf{E}_{in}(\mathbf{r}, t = 0)$ (image to be stored) is mapped onto the atomic ground-state coherence $\rho_{12}(\mathbf{r}, t = 0)$, whose dynamics at storage time t is dominated by[19]

$$\partial_t \rho_{12}(\mathbf{r}, t) - D\nabla_\perp^2 \rho_{12}(\mathbf{r}, t) = 0, \qquad (1)$$

where D is the spatial diffusion coefficient and the retrieved beam's amplitude $|\mathbf{E}_{re}(\mathbf{r}, t)|$ is proportional to $|\rho_{12}(\mathbf{r}, t)|$. Then, we obtain the retrieved image $I_{re}(\mathbf{r}, t)$ derived from Eq. (1) as

$$I_{re}(\mathbf{r}, t) = |\mathbf{E}_{re}(\mathbf{r}, t)|^2 \propto \left| \int \mathbf{E}_{in}(\tilde{\mathbf{r}}, t = 0) e^{-|\mathbf{r} - \tilde{\mathbf{r}}|^2/(4Dt)} d^2\tilde{\mathbf{r}} \right|^2. \qquad (2)$$

Equation (2) indicates that the stored image undergoes a Gaussian attenuation related to t and D, and the larger t or D, the more blurring of the retrieved image.

If an additional phase $\phi(\mathbf{r})$ is loaded onto the input beam ($\mathbf{E}_{in}(\mathbf{r}, t = 0)e^{i\phi(\mathbf{r})}$), and substituting it into Eq. (2), the retrieved image $I_{re}(\mathbf{r}, t)$ would be different. Let $I_{in}(\mathbf{r}, t = 0) = |\mathbf{E}_{in}(\mathbf{r}, t = 0)|^2$, we are committed to find out the optimal $\phi(\mathbf{r})$ such that $I_{in}(\mathbf{r}, t = 0)$ and $I_{re}(\mathbf{r}, t)$ have the highest similarity. The similarity S between the two images is characterized by[1]

$$S = \frac{\sum (I_{in} \odot I_{re})}{\sqrt{\sum (I_{in} \odot I_{in}) \times \sum (I_{re} \odot I_{re})}}, \qquad (3)$$

where $\odot$ stands for entry-wise multiplication and $\sum$ represents the summation of all elements.

The GA is adopted to solve the mathematical model described above, and the specific steps are illustrated by the flow diagram shown in Fig. 1. The entire process divides into four procedures: initialization, ranking, breeding, and mutation. Initialization: the initialization step starts by gridding the whole region of the image to be stored into the discrete matrix, and then, each matrix element is assigned with a random value ranging from 0 to π. Such a matrix forms an initial random phase pattern $\phi_k(\mathbf{r})$, where $k = 1 : N$ (N initial phase patterns generated in this manner). Ranking: substituting each $\phi_k(\mathbf{r})$ into Eq. (2) and the corresponding S can be obtained through Eq. (3), which is the so-called fitness function in GA. Then, these N phase patterns are ranked by S value from high to low, and two of them are selected as parent patterns (*ma* and *pa*) according to the rule that the higher the ranking, the higher possibility to be selected. Breeding: a random binary template T is generated for breeding an offspring, which is described mathematically as *offspring = ma $\odot$ T + pa $\odot$ (1 − T)*. Mutation: several random genes of the offspring (elements marked in red boxes in Fig. 1) are replaced with random numbers from 0 to π. Thereby, a new offspring is generated. The mutation rate R is defined as $R = (R_0 − R_{end})e^{-n/\lambda} + R_{end}$, where R_0 and R_{end} are the initial and final mutation rate, n is the generation number, and λ is the decay factor.[25] The mutation rate is designed to decrease as the generation
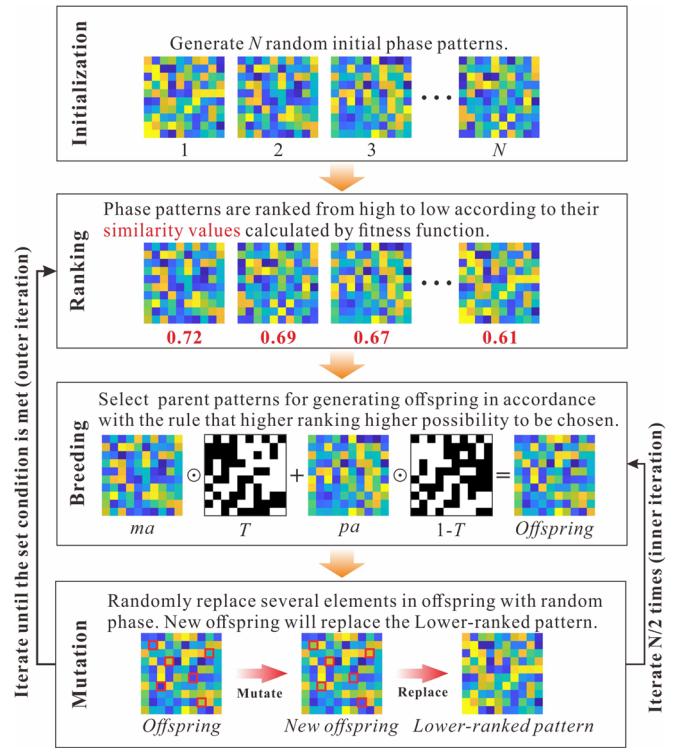

FIG. 1. A flow diagram showing the GA's steps: (1) a population consisting of N random initial phases is created. (2) These phase patterns are ranked by fitness (namely similarity). (3) Two parent patterns (*ma* and *pa*) are selected for breeding. The higher the ranking, the higher the possibility to be selected. An offspring is generated by *ma* and *pa*. (4) The generated offspring mutates and replaces the lower-ranked phase pattern. The process from generation of offspring to mutation to replacement keeps until all the $N/2$ lower-ranked phase patterns are replaced. As a result, a new population is created and then goes back to the second step. Until the set condition is met, the iteration ends.

number increases to prevent over mutation. In this way, $N/2$ new offsprings are generated to replace the original $N/2$ lower-ranked phase patterns. Consequently, a new population is created, consisting of the original $N/2$ top-ranked individuals and $N/2$ mutated offsprings. So far, one iteration completes. The next iteration starts with re-ranking the new population and repeats the "breeding" and the "mutation" steps. After a certain number of iterations, each $\phi_k(\mathbf{r})$ will gradually reach up to optimal and we eventually pick out the best one for the experiment.

To intuitively evaluate this method's performance, we first utilize GA to calculate the optimal phase of a three-line image I_{thr} [Fig. 2(a)] as mentioned in Ref. 21. The image (as well as the other images in the rest of the paper) size is 200×200 pixels with each pixel size of $12.5 \times 12.5\,\mu m^2$. To increase the computing speed of the optimal phase calculation, 20×20 pixels are binned into a super-pixel; thus, the matrix dimension of the phase pattern is 10×10 super-pixels. Other parameters are $N = 200$, $R_0 = 0.2$, $R_{end} = 0.001$, $\lambda = 100$. The temperature and the buffer gas pressure of the vapor cell determine the value of D. In common cases, e.g., $50\,^\circ C$ cell temperature and $10\,Torr$ neon buffer gas, $D \sim 10^{-3}\,m^2/s$, and t is set as a few
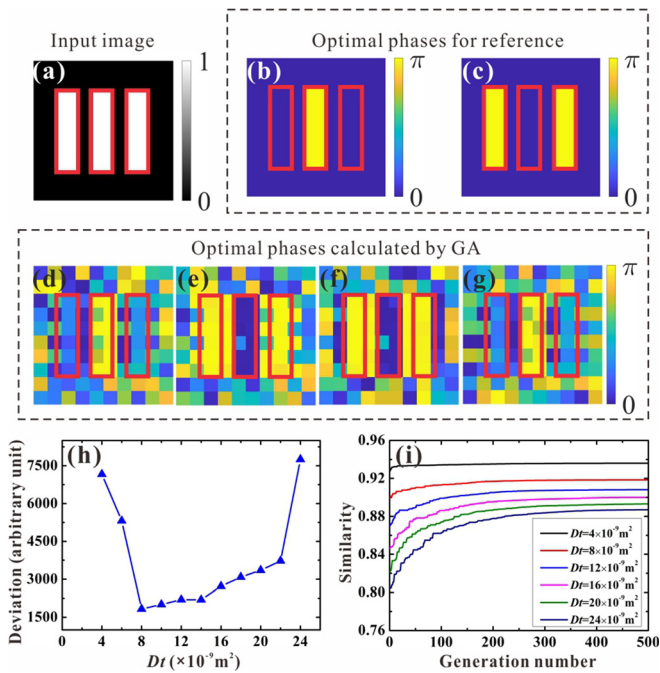
FIG. 2. Optimal phase simulations of a three-line pattern based on GA. (a) The image to be stored. (b) and (c) Optimal phases for reference. (d)–(g) Optimal phases calculated by GA under $Dt = 4 \times 10^{-9}$, 8×10^{-9}, 20×10^{-9}, and 24×10^{-9} m^2, where D and t denote atomic diffusion coefficient and storage time, respectively. (h) The deviation between the calculated optimal phase and the referenced optimal phases vs Dt. (i) Storage similarity against the generation number of GA under different Dt.

microseconds.[21] Thus, we can deduce that their product $Dt \sim 10^{-9} - 10^{-8}$ m^2. Four phase patterns [Figs. 2(d)–2(g)] are calculated through GA with Dt set as 4×10^{-9}, 8×10^{-9}, 20×10^{-9}, and 24×10^{-9} m^2. According to the phase-shift lithography technique,[21] the optimal phase difference between adjacent lines should be π, as can be seen in Figs. 2(b) and 2(c) as a reference. All the phase patterns calculated via the GA approach to the reference phases in Figs. 2(b) and 2(c) but Figs. 2(d) and 2(g) appear a little bit deviated. To quantitatively assess the qualities of the calculated phases, we use the following formula to assess the deviation between the calculated phase (denoted as P^{est}) and the reference phases (denoted as P_1^{ref} and P_2^{ref}): $Deviation = min(\sum |P^{est} - P_1^{ref} \odot I_{thr}|, \sum |P^{est} - P_2^{ref} \odot I_{thr}|)$. The deviation calculation [see Fig. 2(h)] manifests that when Dt varies from 6×10^{-9} to 2.2×10^{-8} m^2, the GA exhibits excellent performance. When Dt exceeds this range, the algorithm performs a little bit worse. It indicates that a good GA optimization performance is not very sensitive to Dt's setting requirement, at least under the condition of a simple image to be stored, meaning that the Dt's selection will become less demanding. Figure 2(i) displays the trend of similarity as the increase in generation number. Evidently, the larger the Dt, the slower the convergence. In general, 500 iterations are enough to obtain the optimal phase. The GA optimization is implemented using MATLAB with a 3.6 GHz Intel Core i7 processor and 8 GB RAM, which takes $\sim$233 s.

To attest that the GA optimization applies to the storage of arbitrary images, we theoretically simulate the storage of four complex images [Fig. 3(a)], and the simulation results are shown in Fig. 3(b). Here $Dt = 6 \times 10^{-9}$ m^2 and other parameters are the same as in Fig. 2. The first row of Fig. 3(b) is obtained by substituting the original input images carrying plane phase fronts ($\phi(\mathbf{r}) = 0$) into Eq. (2). In contrast, the second row is the retrieved images with the optimal phase calculated by GA. Regardless of the minor intensity variations caused by some phase abrupt elements accidentally induced by the GA's random processes (e.g., breeding and mutation), one observe clearly that the retrieved images in the second case are more discernible in detail, manifesting that the phase patterns calculated by GA are helpful for suppressing the image blurring caused by atomic diffusion. The peak signal-to-noise ratio (PSNR) of each retrieved image with respect to the corresponding input image is also given in Fig. 3(c), which can be used for quantitative evaluations of both circumstances. It is obvious that the PSNR of the GA optimization is improved by 0.7 to 1 dB.

Next, we explore the experimental performance of GA assisted image storage in the thermal atomic vapor cell. The experimental setup is exhibited in Fig. 4. A 5 cm long ^{87}Rb atomic gas cell containing 8 Torr neon buffer gas is heated to 60 °C and placed in a magnetically shielded μ-metal oven. The vertically polarized control beam and horizontally polarized probe beam combine and co-propagate through polarizing beam splitter 1 (PBS1). After passing through the vapor cell, they spatially separate by PBS2. The atomic filter (AF), which is an 80 °C atomic cell with all the atoms populated on $|5S_{1/2}, F = 2\rangle$, is used to absorb the residual control beam after PBS2. The control beam and the probe beam are resonantly coupling to $|5S_{1/2}, F = 2\rangle \rightarrow |5P_{1/2}, F' = 1\rangle$ and $|5S_{1/2}, F = 1\rangle \rightarrow |5P_{1/2}, F' = 1\rangle$ transitions, forming the Λ-type electromagnetically induced transparency (EIT) configuration. The two beams are chopped separately by two
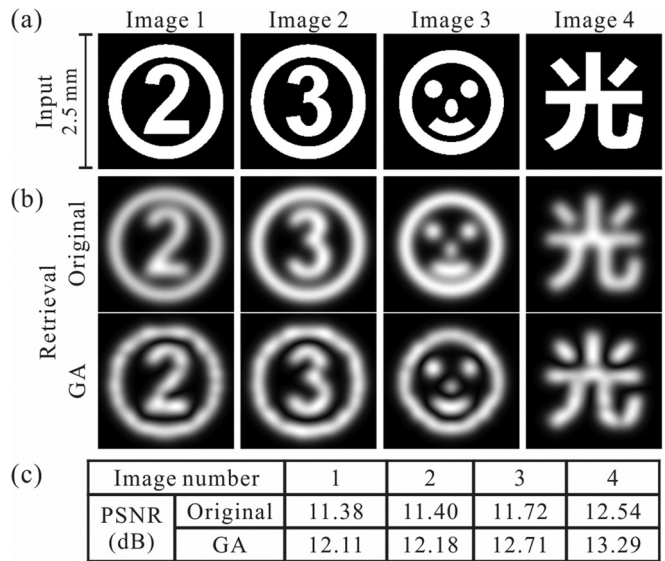

FIG. 3. Simulation results of storing four complex images. (a) The images to be stored. (b) The retrieved images without any modulation (second row, marked as original) and with GA assisted phase modulation (third row, marked as GA) under the case of $Dt = 6 \times 10^{-9}$ m^2. (c) PSNR of the retrieved images.
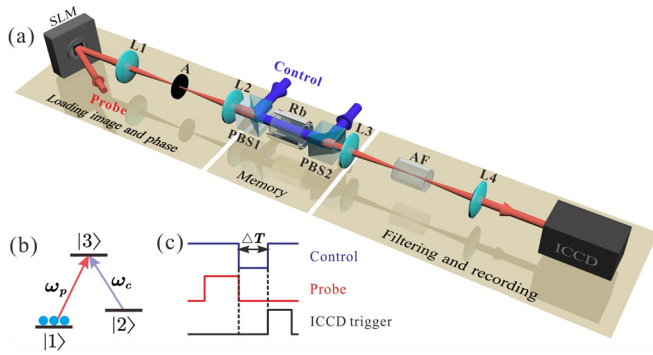
FIG. 4. (a) Experiment setup. Red (blue) line: probe (control) optical path, SLM: spatial light modulator, L1–L4: lenses with a focal length of 500 mm, A: aperture, PBS1 and PBS2: polarizing beam splitters, AF: atomic filter, ICCD: intensified charge-coupled device. (b) Energy level structure. (c) Time sequence.

acousto-optic modulators (not shown in the figure), allowing us to precisely regulate the time sequence shown in Fig. 4(c). The pulse width of the probe beam is 2 μs, and the storage time is denoted as ΔT. When turning off the control beam adiabatically, the probe pulse is stored in the atomic ensemble and will not be released until the control beam is turned on again. The retrieved image is recorded by an intensified charge-coupled device camera (ICCD, Andor iStar 334T) synchronized with the re-opened control. The control is a Gaussian beam with a 6 mm waist, while the probe is modulated by a spatial light modulator (SLM, pixel size $12.5 \times 12.5\,\mu m^2$) into the desired image carrying designed phase structure. For a given image, loading the optimal phase pattern calculated by GA onto it is the core step of our experiment. The related parameters of GA here are the same as those in the previous simulations.

The four images, shown in Fig. 5(a), are stored for 5 μs, and the experimental results are exhibited in Fig. 5(b). All these images are stored under two cases: one is without phase modulation (the second row) and the other is phase modulated by GA (the third row). As expected, the atomic diffusion leads to distortion of the retrieved image, which is revealed in the mixing of adjacent lines. Take the smiling face as an example, its eyes, nose, and mouth disperse and are unrecognizable when stored with no phase modulation. When carrying the optimal phases calculated by GA, the retrieved images possess clearer outlines. Unlike the previous works that can only store periodically distributed transverse images,[11,21] our scheme can store curved lines with the continuous transition. Take the retrieved image "③" as a reference, when carrying the optimal phase, not only there is no crosstalk between "3" and "〇" but also all the corners of 3 are clean-cut. The PSNR values of the retrieved images under the two cases are listed in Fig. 5(c), which shows that the GA optimization obtain a PSNR improvement by 0.8–2 dB. It should mention that due to the low storage efficiency, we only show the retrieved images stored up to 5 μs, but the GA assisted images are able to maintain their profiles much longer than this time.

Furthermore, a more complicated image [see Fig. 6(a)] is stored to quantify the advantage of GA optimization. The retrieved images under incremental storage time are shown in Figs. 6(b)–6(g), in which the original retrieved images suffer disastrous distortions while the retrieved images optimized by GA exhibit a high degree of recognition.
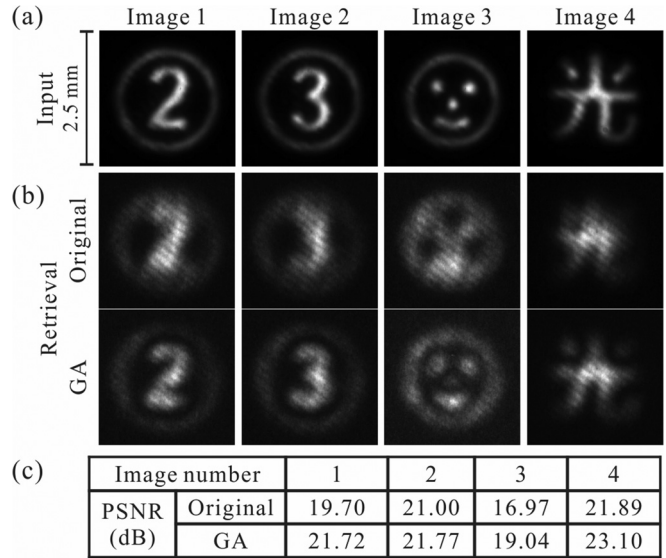

FIG. 5. Experimental storage results of the four images mentioned in Fig. 3. (a) The image to be stored. (b) The retrieved images without any modulation (second row, marked as original) and carrying the optimal phases calculated by genetic algorithm (third row, marked as GA) under the case of $Dt = 6 \times 10^{-9}$ m^2. (c) PSNR of the retrieved images. The storage time fixes as 5 μs.

To compare the two results more clearly, we obtain the normalized intensity distributions along the vertical scanning direction [marked by the red dashed line in Fig. 6(a)], as shown in Figs. 6(h) and 6(i). Apparently, the retrieved signals in Fig. 6(i) (corresponding to GA)
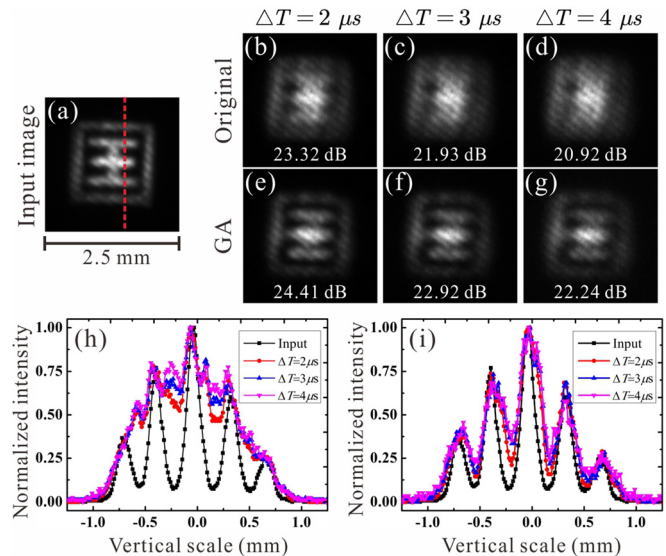

FIG. 6. Experimental storage of a complicated image. (a) The image to be stored. (b)–(d) The original retrieved images with different storage time ΔT. (e)–(g) The retrieved images modified by genetic algorithm (GA) vs ΔT. (h) and (i) Intensity distributions in longitudinal scanning (red dashed line) of (b)–(d) and (e)–(g). The PSNR is marked with a white number.

maintain better profiles, while the original retrieved signals in Fig. 6(h) deviate tremendously from the input image. Moreover, the PSNR values marked in Figs. 6(b)–6(g) indicate that the GA optimization achieves ~1 dB of PSNR improvement on average. It is worth reminding that the optimal phase is easily accessible through the simple mathematical model aforementioned, and there is no need to take the complexity of the image into account, enabling our scheme to be flexibly and effectively applied in the high-resolution storage of arbitrary transverse images.

Though the retrieved images' qualities are improved significantly, we should point out that the performance of GA optimization could be further improved by adjusting the relevant parameters aforementioned. Taking the super-pixel size as an example, in the previous experiments, we combined 20×20 pixels into one super-pixel in order to reduce the computation. This is at the cost of reducing the fineness of the phase structure. We further shrink a super-pixel to 10×10 pixels and compare the storage performance with Fig. 6. The experimental result, in this case, is shown in Fig. 7(d) [Fig. 6(b) is listed in Fig. 7(b) as a reference]. The corresponding optimal phases are also given in Figs. 7(a) and 7(c). The other parameters for calculating Fig. 7(c) are the same for calculating Fig. 7(a) except for the iteration number, which is 1000 due to the increased computation data. Compared with Fig. 7(b), Fig. 7(d) possesses clearer profiles and has a higher PSNR, indicating that a smaller super-pixel size is beneficial to improve the performance of GA optimization. Referring to Figs. 7(a) and 7(c), we can observe that both of the phase structures basically following the principle of π phase shift between adjacent and spatially separated regions, but the phase distributions around the corners are more complex. As shown in the zoom-in phase diagrams marked by the red boxes, the smaller super-pixel size makes the phase structure more refined and is conducive to making the phase difference between adjacent regions closer to π. For instance, the local phase difference corresponding to Fig. 7(c) reaches 0.95π, which is higher than that (0.79π) in Fig. 7(a), thereby increasing the local visibility of the retrieved imag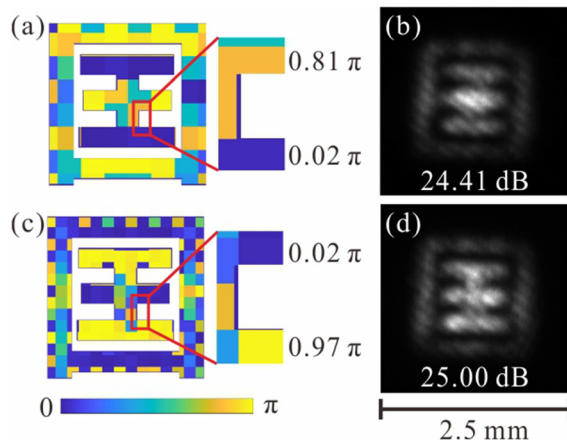e. The influence of other parameters, including the choice of the fitness function, on the GA optimization process, could also be further explored to obtain better storage results.

In conclusion, we demonstrate the application of GA in improving the storage qualities of arbitrary images in the thermal atomic ensemble. We begin by theoretically simulating the storage of a simple three-line image and discuss the influence of several critical parameters in GA optimization. Then, we theoretically and experimentally investigate the storage of four representative images with and without the GA optimization. The results show that the stored images carrying the optimal phases calculated by GA can resist image blurring caused by atomic diffusion and maintain clearer profiles. Finally, the excellent storage results of a more complicated image further prove the high practicability and superiority of GA assisted image storage. Our scheme is universal for increasing the storage fidelity of arbitrary transverse multimode light in the diffusion media and may have broad applications in quantum communications.

DATA AVAILABILITY

The data that support the findings of this study are available from the corresponding author upon reasonable request.

REFERENCES

[1]D.-S. Ding, Z.-Y. Zhou, B.-S. Shi, and G.-C. Guo, "Single-photon-level quantum image memory based on cold atomic ensembles," Nat. Commun. **4**, 2527 (2013).

[2]Y. Wang, J. Li, S. Zhang, K. Su, Y. Zhou, K. Liao, S. Du, H. Yan, and S.-L. Zhu, "Efficient quantum memory for single-photon polarization qubits," Nat. Photonics **13**, 346–351 (2019).

[3]T.-S. Yang, Z.-Q. Zhou, Y.-L. Hua, X. Liu, Z.-F. Li, P.-Y. Li, Y. Ma, C. Liu, P.-J. Liang, X. Li, Y.-X. Xiao, J. Hu, C.-F. Li, and G.-C. Guo, "Multiplexed storage and real-time manipulation based on a multiple degree-of-freedom quantum memory," Nat. Commun. **9**, 3407 (2018).

[4]B. Stiller, M. Merklein, K. Vu, P. Ma, S. J. Madden, C. G. Poulton, and B. J. Eggleton, "Cross talk-free coherent multi-wavelength Brillouin interaction," APL Photonics **4**, 040802 (2019).

[5]A. Grodecka-Grad, E. Zeuthen, and A. S. Sørensen, "High-capacity spatial multimode quantum memories based on atomic ensembles," Phys. Rev. Lett. **109**, 133601 (2012).

[6]C. Simon, H. de Riedmatten, M. Afzelius, N. Sangouard, H. Zbinden, and N. Gisin, "Quantum repeaters with photon pair sources and multimode memories," Phys. Rev. Lett. **98**, 190503 (2007).

[7]L. Allen, M. W. Beijersbergen, R. J. C. Spreeuw, and J. P. Woerdman, "Orbital angular momentum of light and the transformation of Laguerre-Gaussian laser modes," Phys. Rev. A **45**, 8185–8189 (1992).

[8]M. A. Bandres and J. C. Gutiérrez-Vega, "Ince–Gaussian beams," Opt. Lett. **29**, 144–146 (2004).

[9]Yao-Li, X.-B. Hu, B. Perez-Garcia, Bo-Zhao, W. Gao, Z.-H. Zhu, and C. Rosales-Guzman, "Classically entangled Ince–Gaussian modes," Appl. Phys. Lett. **116**, 221105 (2020).

[10]J. Wang, F. Castellucci, and S. Franke-Arnold, "Vectorial light–matter interaction: Exploring spatially structured complex light fields," AVS Quantum Sci. **2**, 031702 (2020).

[11]P. K. Vudyasetu, R. M. Camacho, and J. C. Howell, "Storage and retrieval of multimode transverse images in hot atomic rubidium vapor," Phys. Rev. Lett. **100**, 123903 (2008).

[12]L. Wang, Y.-H. Sun, R. Wang, X.-J. Zhang, Y. Chen, Z.-H. Kang, H.-H. Wang, and J.-Y. Gao, "Storage of airy wavepackets based on electromagnetically induced transparency," Opt. Express **27**, 6370–6376 (2019).

FIG. 7. Experimental comparison of optimization performance under different pixel binning. (a) and (b) correspond to the case of 20×20 pixel binning. (c) and (d) correspond to the case of 10×10 pixel binning. The first and second columns are the optimal phase patterns calculated by GA and the retrieved images, respectively. The PSNR is marked with a white number.

[13]D.-S. Ding, J.-H. Wu, Z.-Y. Zhou, B.-S. Shi, X.-B. Zou, and G.-C. Guo, "Multiple image storage and frequency conversion in a cold atomic ensemble," Phys. Rev. A **87**, 053830 (2013).

[14]V. Parigi, V. D'Ambrosio, C. Arnold, L. Marrucci, F. Sciarrino, and J. Laurat, "Storage and retrieval of vector beams of light in a multiple-degree-of-freedom quantum memory," Nat. Commun. **6**, 7706 (2015).

[15]D.-S. Ding, W. Zhang, Z.-Y. Zhou, S. Shi, G.-Y. Xiang, X.-S. Wang, Y.-K. Jiang, B.-S. Shi, and G.-C. Guo, "Quantum storage of orbital angular momentum entanglement in an atomic ensemble," Phys. Rev. Lett. **114**, 050502 (2015).

[16]Y.-W. Cho, J.-E. Oh, and Y.-H. Kim, "Diffusion-free image storage in hot atomic vapor," Phys. Rev. A **86**, 013844 (2012).

[17]Y. Yu, Y. Chen, C. Wang, J. Wang, Z. Sun, M. Cao, H. Gao, and F. Li, "Optical storage of Ince–Gaussian modes in warm atomic vapor," Opt. Lett. **46**, 1021–1024 (2021).

[18]K. Ishikawa and T. Yabuzaki, "Diffusion coefficient and sublevel coherence of Rb atoms in N_2 buffer gas," Phys. Rev. A **62**, 065401 (2000).

[19]O. Firstenberg, M. Shuker, A. Ron, and N. Davidson, "Colloquium: Coherent diffusion of polaritons in atomic media," Rev. Mod. Phys. **85**, 941–960 (2013).

[20]R. Chriki, S. Smartsev, D. Eger, O. Firstenberg, and N. Davidson, "Coherent diffusion of partial spatial coherence," Optica **6**, 1406–1411 (2019).

[21]M. Shuker, O. Firstenberg, R. Pugatch, A. Ron, and N. Davidson, "Storing images in warm atomic vapor," Phys. Rev. Lett. **100**, 223601 (2008).

[22]S. Smartsev, R. Chriki, D. Eger, O. Firstenberg, and N. Davidson, "Structured beams invariant to coherent diffusion," Opt. Express **28**, 33708–33717 (2020).

[23]C. M. Anderson-Cook, "Practical genetic algorithms," J. Am. Stat. Assoc. **100**, 1099 (2005).

[24]Y. Luo, S. Yan, H. Li, P. Lai, and Y. Zheng, "Focusing light through scattering media by reinforced hybrid algorithms," APL Photonics **5**, 016109 (2020).

[25]D. B. Conkey, A. N. Brown, A. M. Caravaca-Aguirre, and R. Piestun, "Genetic algorithm optimization for focusing through turbid media in noisy environments," Opt. Express **20**, 4840–4849 (2012).

[26]X. Zhang and P. Kner, "Binary wavefront optimization using a genetic algorithm," J. Opt. **16**, 125704 (2014).

[27]D. M. Deaven and K. M. Ho, "Molecular geometry optimization with a genetic algorithm," Phys. Rev. Lett. **75**, 288–291 (1995).

[28]W. Rohringer, R. Bücker, S. Manz, T. Betz, C. Koller, M. Göbel, A. Perrin, J. Schmiedmayer, and T. Schumm, "Stochastic optimization of a cold atom experiment using a genetic algorithm," Appl. Phys. Lett. **93**, 264101 (2008).